catalysts

MDPI

Article

Physico-Chemical and Catalytic Properties of Mesoporous CuO-ZrO_2 Catalysts

Sulaiman N. Basahel [1], Mohamed Mokhtar [1], Edreese H. Alsharaeh [2], Tarek T. Ali [1,3,*], Hatem A. Mahmoud [3,4] and Katabathini Narasimharao [1,*]

[1] Chemistry Department, Faculty of Science, King Abdulaziz University, Jeddah 21589, Saudi Arabia; sbasahel@hotmail.com (S.N.B.); mmokhtar2000@yahoo.com (M.M.)

[2] Chemistry Department, College of Science & General Studies, Alfaisal University, Riyadh 11533, Saudi Arabia; ealsharaeh@alfaisal.edu

[3] Chemistry Department, Faculty of Science, Sohag University, Sohag, P.O. Box 82524, Egypt; hatem_elnakeeb@yahoo.com

[4] Chemistry Department, College of Science, University of Hail, Hail 81451, Saudi Arabia

* Correspondence: catalysa98@yahoo.com (T.T.A.); nkatabathini@kau.edu.sa (K.N.); Tel.: +966-569570912 (T.T.A.); +966-538638994 (K.N.); Fax: +966-26952292 (K.N.)

Academic Editor: Keith Hohn

Received: 2 February 2016; Accepted: 31 March 2016; Published: 13 April 2016

Abstract: Mesoporous CuO-ZrO_2 catalysts were prepared and calcined at 500 °C. The performance of the synthesized catalysts for benzylation of benzene using benzyl chloride was studied. The bare support (macroporous ZrO_2) offered 45% benzyl chloride conversion after reaction time of 10 h at 75 °C. Significant increase in benzyl chloride conversion (98%) was observed after CuO loading (10 wt. %) on porous ZrO_2 support. The conversion was decreased to 80% with increase of CuO loading to 20 wt. %. Different characterization techniques (XRD, Raman, diffuse reflectance UV-vis, N_2-physisorption, H_2-TPR, XPS and acidity measurements) were used to evaluate physico-chemical properties of CuO-ZrO_2 catalysts; the results showed that the surface and structural characteristics of the ZrO_2 phase as well as the interaction between CuO-ZrO_2 species depend strongly on the CuO content. The results also indicated that ZrO_2 support was comprised of monoclinic and tetragonal phases with macropores. An increase of the volume of monoclinic ZrO_2 phase was observed after impregnation of 10 wt. % of CuO; however, stabilization of tetragonal ZrO_2 phase was noticed after loading of 20 wt. % CuO. The presence of low-angle XRD peaks indicates that mesoscopic order is preserved in the calcined CuO-ZrO_2 catalysts. XRD reflections due to CuO phase were not observed in case of 10 wt. % CuO supported ZrO_2 sample; in contrast, the presence of crystalline CuO phase was observed in 20 wt. % CuO supported ZrO_2 sample. The mesoporous 10 wt. % CuO supported ZrO_2 catalyst showed stable catalytic activity for several reaction cycles. The observed high catalytic activity of this catalyst could be attributed to the presence of a higher number of dispersed interactive CuO (Cu^{2+}-O-Zr^{4+}) species, easy reducibility, and greater degree of accessible surface Lewis acid sites.

Keywords: CuZr nanocomposite; Cu^{2+}-O-Zr^{4+} species; dispersion; acid sites; benzylation

1. Introduction

Zirconium oxide (ZrO_2) has been used as a catalyst and support mainly because of its unique properties as it can possess relatively high surface area, the preservation of both acid and basic sites and possession of redox properties [1]. It is also mechanically and thermally stable; as a result, ZrO_2 has been used as a structural promoter and, more frequently, as a support material in many catalytic applications. CuO-ZrO_2 materials were used as catalysts for many reactions such as methanol decomposition [2], oxidative steam reforming of methanol, NO, N_2O decomposition, CO and CO_2 hydrogenation [3–5].

It was reported that ZrO_2 favors the dispersion and reducibility of CuO and can influence the adsorption and activation of reactants [6]. Understanding the local structure of CuO-ZrO_2 catalysts, interaction between active metal oxide and support and the factors that determine the formation of the active phase are the important aspects in the development of ZrO_2 based catalysts for heterogeneous catalytic applications [7]. The nature of interactions between active phase and ZrO_2 support has been extensively studied in the literature [8–10], this is mainly because of the properties of metal oxide supported ZrO_2 catalysts: they often show different catalytic properties compared to those of the corresponding bulk metal oxides due to the interaction between metal oxide and support. It was also shown that the ZrO_2 phases influence the catalytic performance. Qu *et al.* [11] reported that CuO supported monoclinic ZrO_2 catalysts are more active in methanol synthesis than CuO supported tetragonal ZrO_2. However, characterization of the surface structure of supported ZrO_2 catalysts yields a complex and controversial information, since different structures and chemical states could exist in metal oxide supported ZrO_2 catalysts. In the present work, we studied the physico-chemical properties of synthesized porous CuO-ZrO_2 catalysts to understand the nature of interaction between CuO and ZrO_2, which coexisted with monoclinic and tetragonal phases.

CuO-ZrO_2 catalysts can be prepared using different preparation methods such as sol-gel, impregnation, and co-precipitation. The structural properties and catalytic activities of the materials obtained using these techniques varied substantially [12]. The development of highly active solid reusable heterogeneous catalysts for the Friedel-Crafts alkylation reactions gained large practical importance. Researchers have used different solid catalysts, such as zeolites [13], Fe-MCM-41 [14], Fe-HMS [15] and clays exchanged with metallic ions [16] for benzylation of benzene. It was observed that catalysts with mesoporous showed higher activity in benzylation compared to catalysts which are microporous in nature. However, the reported mesoporous catalysts have low stability and weak acidity compared to those of zeolite samples. Therefore, development of stable mesoporous catalysts with strong acidity for benzylation is a topic of interest [17].

Cseri *et al.* [18] performed benzylation of aromatic compounds with benzyl chloride using a series of ion exchanged clays as catalysts and the authors observed that the clays with Fe^{3+}, Sn^{4+} and Cu^{2+} ions showed very good activities. Bachari and Cherifi [19] also studied the benzylation reaction using benzyl chloride using CuO supported HMS catalysts with different CuO loadings. The authors observed that bare HMS support and Cu supported HMS catalysts with low Cu loading were totally inactive; benzylation activity was observed after increase of Cu loading over HMS support. However, the catalysts which contained high Cu content offered high benzyl chloride conversions but low diphenylmethane selectivity.

In a recent publication [20], we synthesized mesoporous iron and nickel oxide supported ZrO_2 by a simple co-precipitation method. Formation of highly dispersed Fe^{3+}-ZrO_2 interactive species were observed in case of 20 wt. % iron oxide supported ZrO_2 catalyst. In contrast, the nickel oxide was agglomerated on the ZrO_2 surface and formed as segregated crystalline nickel oxide due to its weak interaction with ZrO_2 support. We are interested in developing stable solid acid catalysts for different chemical reactions. As part of our continued research, we synthesized ordered mesoporous CuO-ZrO_2 catalysts and studied their structural properties to investigate the nature of interaction between CuO and ZrO_2 and its role in benzylation of benzene. To the best our knowledge, no report exists on the synthesis of ordered mesoporous CuO-ZrO_2 catalysts with high CuO content (10 and 20 wt. %) and their utilization for benzylation of benzene.

2. Results and Discussion

The low angle XRD patterns were obtained for bare ZrO_2 and CuO-ZrO_2 nanocomposite samples in order to record the mesoporous nature of the materials. As observed in Figure 1A, ZrO_2 sample show well-defined and relatively broad diffraction peaks centered at 2θ of 2°, which indicates the presence of mesopores in the pure ZrO_2 support. It is known that XRD reflections appear at low angles due to regular separation between single channel walls [21]. The presence of low-angle XRD peak in

both calcined CuO-ZrO_2 materials indicates that mesopores were preserved in these samples. The broad shape and lower intensity of the low angle diffraction peak for the samples suggests that the synthesized materials possessed mesopores with a small coherent domain size.

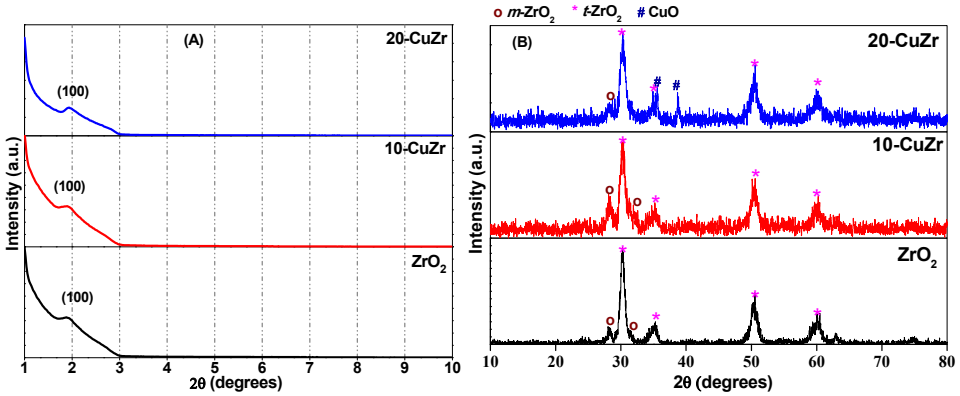

Figure 1. (**A**) Low angle X-ray diffraction (XRD) (**B**) High angle XRD patterns of the samples.

High angle XRD patterns of bare ZrO_2 support and calcined CuO-ZrO_2 nanocomposite samples are shown in Figure 1B. Broad and intense diffraction peaks at 2θ = 30.2°, 35.2°, 50.6° and 60.2° corresponding to the tetragonal phase of ZrO_2 (JCPDS 80-0965) along with a minor peak at 2θ = 28.2° corresponding to major reflection of monoclinic ZrO_2 phase (JCPDS 37-1484) could be observed for bare ZrO_2 support. No reflections due to crystalline CuO phase were observed in XRD pattern of 10-CuZr sample, suggesting that CuO might be well dispersed on the surface of ZrO_2 support. There is a possibility that the absence of crystalline CuO reflections in the high angle XRD pattern for 10-CuZr sample as the particles might be less than 4 nm in size, which is below the detection range of XRD technique. In addition to the characteristic reflections of tetragonal and monoclinic ZrO_2 phases, reflections corresponding to crystalline CuO (tenorite) phase (JCPDS 48-1548) at 2θ = 35.5° and 38.7° were observed for 20-CuZr sample. Broad X-ray diffraction reflections are observed for all the samples, pointing to nanocrystalline nature of ZrO_2.

The change in the ZrO_2 phase with CuO loading was determined by calculating the volume percent of monoclinic and tetragonal ZrO_2 phases presented in the samples. We used the Equations (1) and (2) reported in the literature [22] to calculate volume percent of monoclinic and tetragonal ZrO_2 phases.

$$v_m = \frac{1.311X_m}{1 + (0.311)X_m} \quad (1)$$

where, v_m is volume fraction of the monoclinic phase and that of tetragonal phase is $v_t = 1 - v_m$ and X_m can be calculated by Equation (2)

$$X_m = \frac{I_m(\bar{1}11)}{I_m(\bar{1}11) + I_t(101)} \quad (2)$$

where, I_m ($\bar{1}11$) is the line intensity of the ($\bar{1}11$) reflection (at 2θ = 28.2°) for the monoclinic phase (m-ZrO_2) and I_t (101) is the intensity of the reflection (101) (at 2θ = 30.2°) for tetragonal phase (t-ZrO_2) of the synthesized samples.

The percentages of monoclinic and tetragonal phases were found to be 10.3% and 89.7% respectively for bare ZrO_2 support sample (Table 1). It is interesting to note that, after impregnating 10 wt. % CuO, the volume percentage of monoclinic ZrO_2 phase increased to 27.4% and with further increase of CuO loading to 20 wt. %, it decreased to 4.4%. This observation indicates that the amount of CuO has an influence on the stabilization of ZrO_2 phase. Dongare *et al.* [23] prepared CuO-ZrO_2

catalysts by sol-gel method and observed that Cu content from 2–20 mol% in CuO-ZrO_2 catalysts stabilized the ZrO_2 in cubic fluorite structure. The observed difference in the final phase of CuO-ZrO_2 catalysts could be due to the adaptation of different preparation methods.

Table 1. Results from XRD and H_2-Temperature programmed reduction (H_2-TPR) measurements.

Catalyst	Phase Composition (vol %) [a]		Crystallite Size (nm) [a]		Hydrogen Uptake (mmol·g^{-1}) [b]
	V_m	V_t	*m*-ZrO_2	*t*-ZrO_2	
ZrO_2	10.3	89.7	26.06	20.92	0.05
10-CuZr	27.4	72.6	26.06	20.92	0.45
20-CuZr	4.4	95.6	26.06	17.44	0.59

[a] XRD analysis; [b] H_2-TPR analysis.

The average crystallite size of bare ZrO_2, 10-CuZr and 20-CuZr samples were calculated using Scherrer's equation (Table 1). The calculated average crystallite size of monoclinic and tetragonal phases of all the samples was 24 nm for bare ZrO_2. The average particle size of ZrO_2 remained same after loading 10 wt. % CuO. However, a decrease of particle size (22 nm) was observed in the case of the 20-CuZr sample.

Raman spectroscopy is a well-known technique to distinguish the changes in ZrO_2 phases. Yamamoto *et al.* [24] reported that the tetragonal ZrO_2 phase shows a strong Raman band at 263 cm^{-1} and several other bands at 148, 325, 472, 608 and 640 cm^{-1}. On other hand, the monoclinic ZrO_2 phase shows strong bands at 173, 185 and 472 cm^{-1} and some other bands at 140, 216, 260, 301, 328, 342, 500, 553 and 632 cm^{-1} [25]. The Raman spectra for all the samples are shown in Figure S1 (supporting information). The bare ZrO_2 and 10-CuZr samples showed strong bands corresponding to both tetragonal and monoclinic ZrO_2 phases, indicating the coexistence of both phases in these two samples. The Raman spectrum of 20-CuZr sample showed low intense minor bands due to the monoclinic ZrO_2 phase and high intense major bands due to the tetragonal ZrO_2 phase. The intensity of the Raman bands due to monoclinic ZrO_2 is very low as the volume percentage (calculated from XRD results) for monoclinic ZrO_2 is very small. These results are in accordance with the XRD results.

It was reported that nine Raman bands with different symmetries ($4A_u + 5B_u + A_g + 2B_g$) are possible for the crystalline CuO phase. However, only three ($A_g + 2B_g$) modes are Raman active [26]. Xu *et al.* [27] observed three Raman bands at 282, 330 and 616 cm^{-1} for CuO nanomaterial. It is interesting that we have not observed any bands due to presence of CuO particles in the Raman spectrum of 20-CuZr sample, even though XRD pattern of this sample showed reflections due to crystalline CuO. Xu *et al.* [27] also reported that the intensity Raman bands due to CuO phase is related to the particle size. Stronger and sharper Raman bands could be observed for larger CuO particles and, in addition, bands could shift to longer wavenumbers with increasing CuO particle size. The absence of Raman bands due to CuO phase indicates that some of the impregnated CuO could have deposited inside the pores of the ZrO_2.

Information corresponding to the coordination and different oxidation states of metal (Cu and Zr) ions presented in the samples was studied by diffuse reflectance UV-vis spectroscopy by measuring the *d-d* transitions and oxygen-metal ion charge-transfer bands. Figure 2 shows DR UV-vis spectra for bare ZrO_2 and CuZr nanocomposite samples. Sahu *et al.* [28] reported that ZrO_2 support showed the main absorption band to be located at 228 nm and a broad shoulder around 275 nm. In the present study, the bare ZrO_2 support showed two absorption bands at 230 nm and 275 nm; therefore, these two bands can be assigned to inter band and low-coordinated surface $O^{2-} \rightarrow Zr^{4+}$ transitions respectively in tetragonal and monoclinic ZrO_2. This observation is in good agreement with the XRD results (Figure 1B). The spectrum of 20-CuZr sample showed absorption features in 290–500 nm region and above 720 nm, much different from the spectrum of bare ZrO_2 support. The observed peaks for 20-CuZr sample are mainly due to $O^{2-} \rightarrow Cu^{2+}$ charge transfer (CT) and *d-d* transitions in oligomeric Cu-O-Cu species and CuO crystallites, respectively [29]. The absorption band centered at

around 550 nm for 10-CuZr sample could be assigned to highly dispersed Cu^{2+} ions situated in an octahedral environment [30]. Interestingly, the 10-CuZr sample did not exhibited the absorption peaks around 250 nm and above 740 nm, typical for *d-d* transitions for $O^{2-} \rightarrow Cu^{2+}$ CT in CuO crystallites. The observed differences in DR UV-vis spectra of 10-CuZr sample is due to the presence of finely dispersed Cu species on porous ZrO_2 support, which is approximately in accordance with XRD and Raman spectroscopy results. The above results reveal that in the 10-CuZr sample, the dispersed CuO species dominates, while isolated Cu^{2+} and crystalline CuO coexist in 20-CuZr sample.

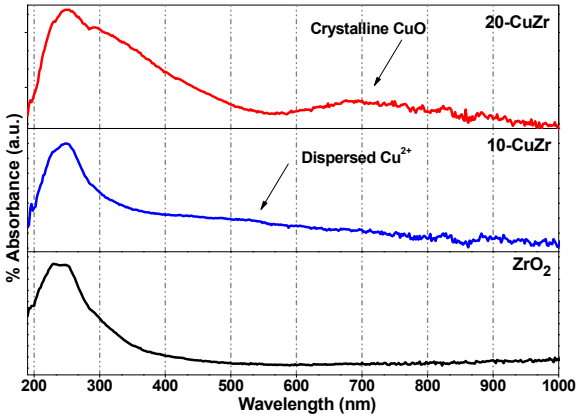

Figure 2. Diffuse reflectance UV-vis (DR UV-vis) spectra for all the samples.

The morphology of synthesized porous ZrO_2 and CuO-ZrO_2 samples was studied by SEM analysis. SEM images (Figure 3) of the samples did not show any major differences; however, SEM analysis is useful to determine the particle size and elemental composition at specific regions of the particles. It can be observed that samples possessed irregular spherical shaped particles with size in the range of 40 to 100 nm. The morphology of ZrO_2 and CuO-ZrO_2 composite powders was uneven and agglomerated. The samples had also been examined by EDX technique (Figure S2), where two distinct phases, Cu and ZrO_2 were clearly observed.

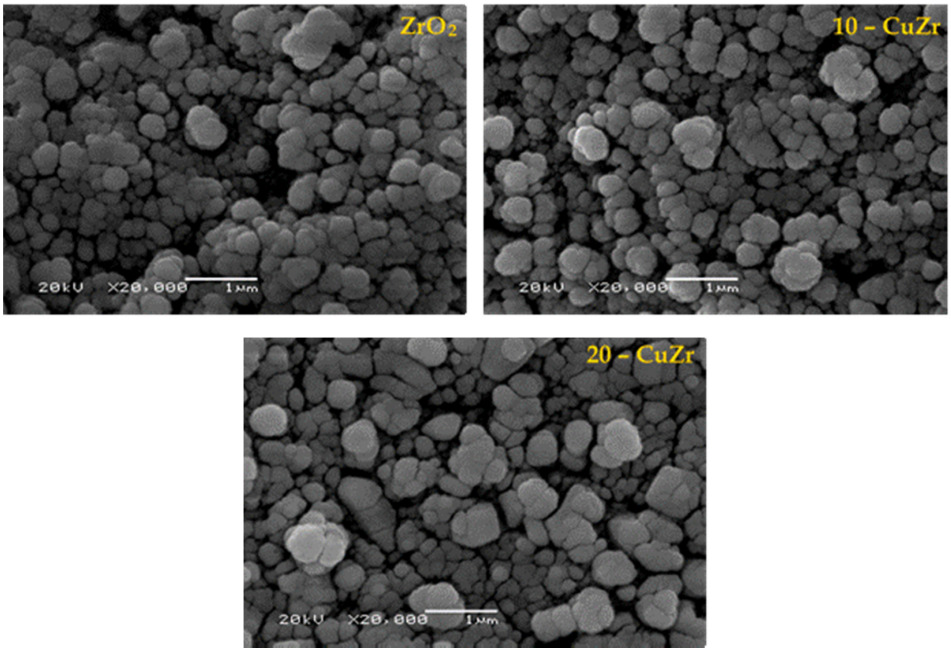

Figure 3. SEM images of ZrO_2 and CuO-ZrO_2 samples.

Figure 4 represents N_2 adsorption-desorption isotherms with the pore size distribution patterns being shown in the inset for ZrO_2 and CuZr samples. The textural properties of the samples are tabulated in Table 2. All the synthesized samples showed type II isotherm with an H3 type hysteresis loop typical of macroporous materials. Bare ZrO_2 sample possessed a specific surface area of 64 $m^2 \cdot g^{-1}$ with large pore size distribution ranging from 7 to 200 nm. With impregnation of CuO, a decrease of specific surface area and pore size was observed. This observation suggests that partial pore blocking occurs with impregnation of CuO. This effect is small in case of 10-CuZr sample, this could be due to the dominant deposition of finely dispersed CuO species on the surface of ZrO_2 support. Significant decrease in the pore volume (from 0.3342 to 0.2413 $cm^3 \cdot g^{-1}$) and specific surface area (from 59 to 45 $m^2 \cdot g^{-1}$) after 20 wt. % CuO loading. This result clearly indicates that crystalline CuO species presented in the 20-CuZr block the ZrO_2 macropores.

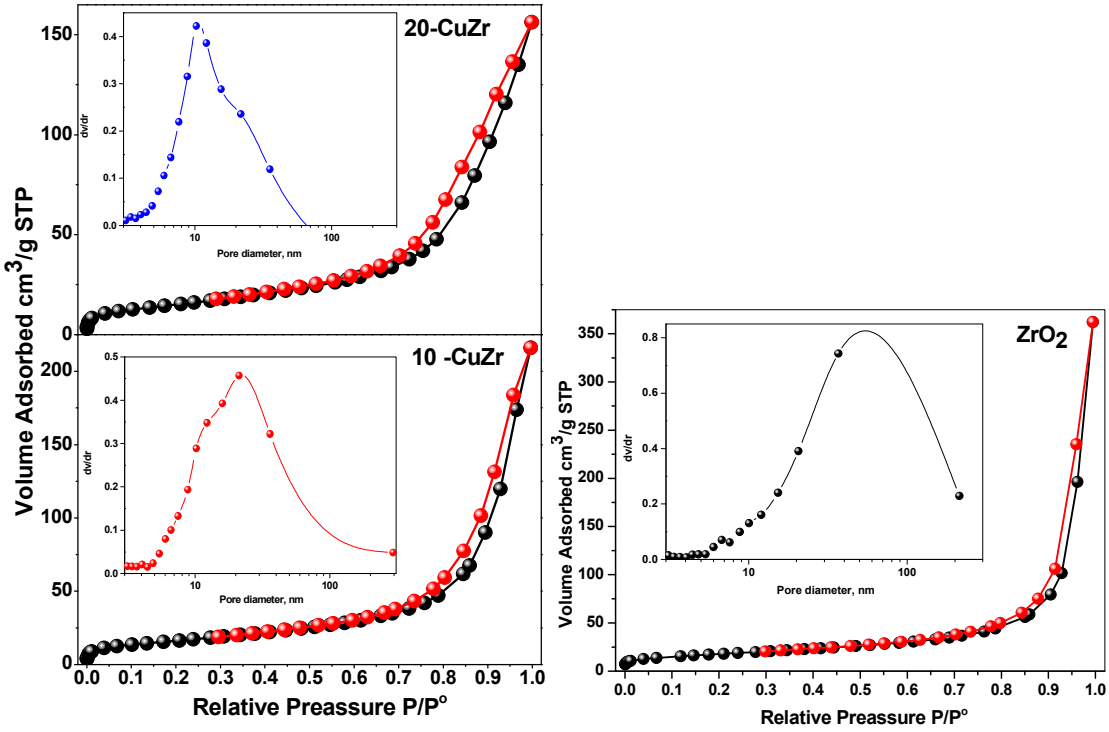

Figure 4. Nitrogen adsorption-desorption isotherms for all the samples (inset pore size distribution patterns).

Table 2. Results from N_2-physisorption, ICP-AES and XPS analysis of the samples.

Catalyst	S_{BET} ($m^2 \cdot g^{-1}$)	V_p ($cm^3 \cdot g^{-1}$)	Av. Pore Diameter (nm)	ICP-AES Chemical Analysis [a] (mass%)		XPS Chemical Analysis [b] (mass%)	
				Zr	Cu	Zr	Cu
ZrO_2	64	0.5619	54	66.6	-	67.8	-
10-CuZr	59	0.3342	23	57.9	7.8	59.4	5.6
20-CuZr	45	0.2413	17	51.5	15.8	52.6	12.5

[a] Bulk composition; [b] Surface composition.

H_2-TPR analysis was used to determine the reduction behavior of the catalysts and also understand the interaction between CuO and ZrO_2. Figure 5 shows H_2-TPR profiles of calcined ZrO_2 and CuO-ZrO_2 samples along with the H_2-TPR profile of bulk CuO sample for comparison. The ZrO_2 sample did not exhibit any reduction peak below 600 °C. On other hand, bulk CuO sample produced a broad reduction peak in the range of 220–420 °C. The H_2-TPR profile of 10-CuZr sample showed two reduction peaks: the first peak appeared at 250 °C and second one at 345 °C. The 20-CuZr sample also showed two reduction peaks, but at different temperatures, first peak was appeared at

235 °C and second one is at 380 °C. In addition, the intensities of the peaks for 20-CuZr sample is higher and broader than the peaks observed for 10-CuZr sample. It is clear that the reduction of Cu species in the CuO-ZrO_2 samples occurred at lower temperatures compared with pure CuO, suggesting that ZrO_2 promotes the dispersion of CuO and enhances the reducibility of Cu species, which is in good agreement with the reported literature [31].

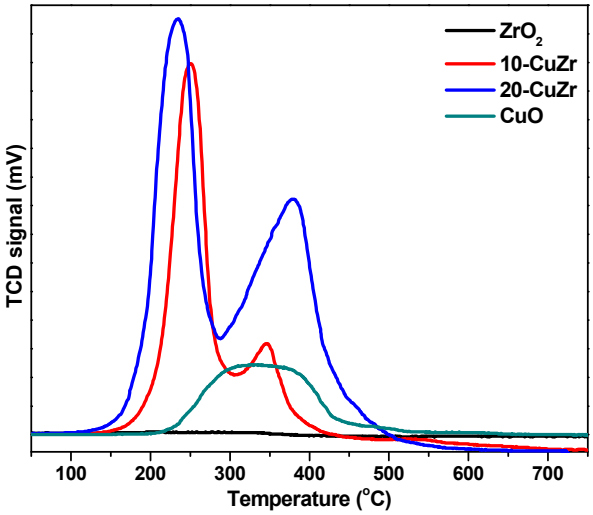

Figure 5. H_2-TPR patterns of all the samples.

The appearance of two reduction peaks in the H_2-TPR profiles of CuO-ZrO_2 samples instead of the single broad peak as observed in pure CuO suggests that CuO-ZrO_2 samples possessed presence of more than one copper oxide species. The first peak at lower temperature for CuO-ZrO_2 samples could be attributed to the reduction of isolated copper oxide particles and the second peak at high temperature can be assigned to highly dispersed Cu species, which are interacted with the ZrO_2 support as well as to well-crystallized CuO in weak interaction with ZrO_2 [32].

The first reduction peak appears at a much lower temperature (235 °C) for 20-CuZr sample. In contrast, the second peak appears at a lower temperature for 10-CuZr sample (345 °C). Usually, dispersed CuO reduces more easily than larger CuO particles; however, it was reported that the interaction between CuO and ZrO_2 depends on the CuO dispersion and crystallinity as well as on the ZrO_2 phase. It was also observed that CuO-supported tetragonal ZrO_2 exhibited an intensive peak, but in a lower temperature region compared to CuO-supported amorphous ZrO_2 and CuO-supported monoclinic ZrO_2. These results demonstrate that the CuO loading affects the dispersion state of the CuO species. Total hydrogen uptake values are presented in Table 1, the total hydrogen uptake was observed to be in the order: 10-CuZr > 20-CuZr > ZrO_2, which indicates that H_2 uptake is influenced by the CuO loading and its interaction with ZrO_2 support. Liu *et al.* [33] observed similar results that indicated that CuO-ZrO_2 catalysts showed two TPR peaks; the high temperature peak could be due to the CuO, which was strongly interacted with ZrO_2 and the lower temperature peak to the CuO which has little interaction with ZrO_2. Based on these observations, the increase of the peak temperature with CuO loading indicates diminishing interaction between the Cu oxide and ZrO_2.

The chemical states of Cu, Zr and O atoms in the catalysts were evaluated by XPS technique. Cu *2p*, CuLMM Auger, Zr *3d* and O *1s* XP spectra for ZrO_2 and CuZr samples are shown in Figure 6A–D respectively. A shake-up satellite at about 942 eV was clearly observed in both CuZr samples, which suggests the presence of Cu^{2+} species in these samples, irrespective of the CuO loading. Furthermore, appearance of Cu $2p_{3/2}$ at 934 eV with consistent satellite peak also suggests a contribution of tenorite CuO phase, which is in accordance with the XRD results. It was reported that Cu^+ or Cu^0 species generally do not show any satellite peaks due to completely filled *3d* shells [34].

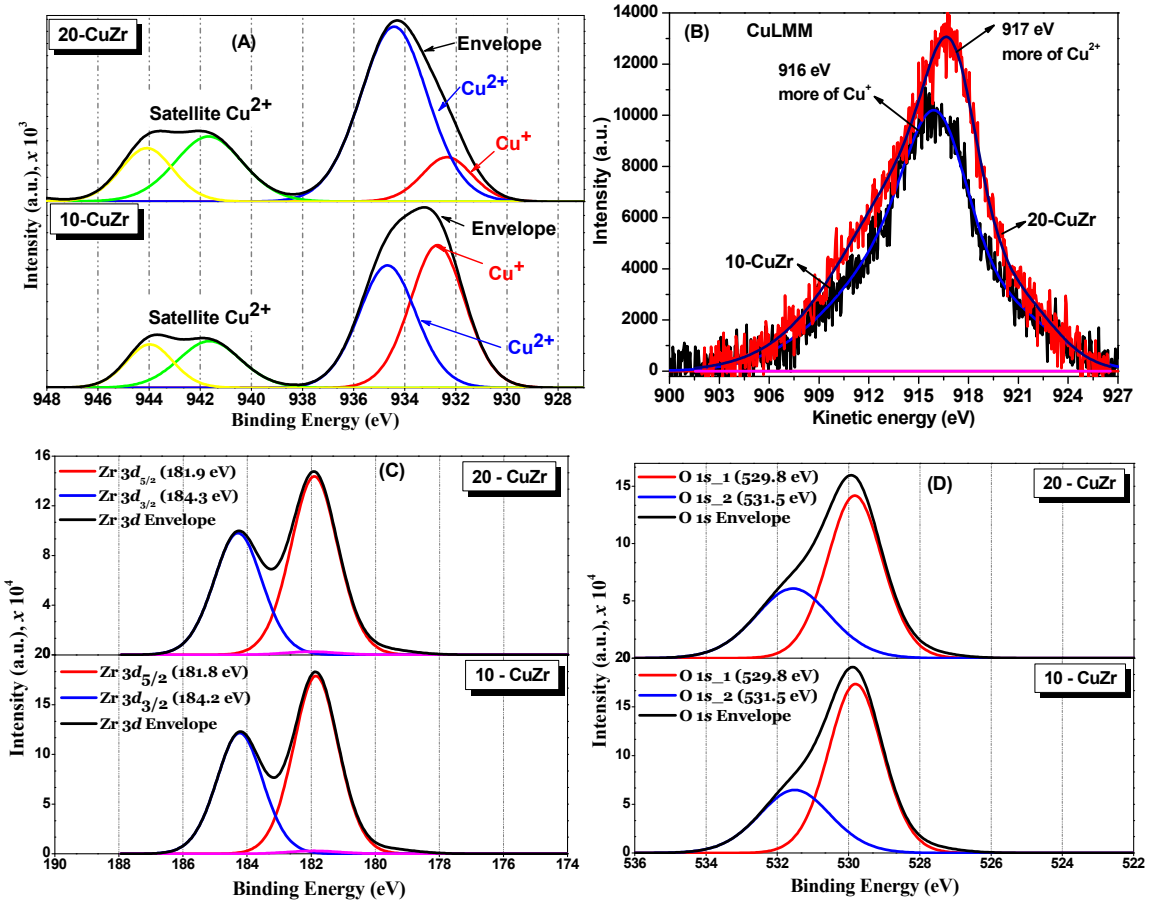

Figure 6. (**A**) Cu *2p* (**B**) CuLMM Auger (**C**) Zr *3d* and (**D**) O *1s* XP spectra for CuZr samples.

Deconvolution of Cu $2p_{3/2}$ XP peaks suggests the presence of two kinds of Cu species in their chemical environments. From the curve fitting, the binding energies (BE) of the two Cu $2p_{3/2}$ components at two different BE (932.2 eV and 935.2 eV) were obtained. The Cu $2p_{3/2}$ XP peak at 935.2 eV can be assigned to bulk CuO species [35]. The other peak at 932.2 eV therefore belongs to species such as Cu^+ or Cu^0. It was reported that distinguishing Cu^0 and Cu^+ species is quite difficult, because their BE values are so close (0.1 eV difference) that they overlap each other [34]. However, we do not believe there is Cu^0 in 10-CuZr and 20-CuZr samples due to the calcination being carried out under the air.

The X-ray induced Cu LMM Auger peaks for 10-CuZr and 20-CuZr samples were obtained in high resolution energy mode to check the presence of Cu^+ and Cu^0. The CuLMM Auger spectra for 10-CuZr and 20-CuZr samples can be seen in Figure 6B. A difference can be observed in the kinetic energy maximum of CuLMM Auger photoelectron spectra of the CuZr samples (10-CuZr: 916 eV and 20-CuZr: 917 eV), most probably due to the difference in interaction at the interface between the ZrO_2 and CuO. It was reported that Cu^{2+} species have a kinetic energy of the Auger transition at *ca.* 917–918 eV [36]. The transitions at 913–914 eV and 918.8–919.3 eV were assigned to CuO aggregates and Cu^0 species, respectively [37]. These observations indicated that 20-CuZr sample possessed Cu^{2+} species.Oon other hand, 10-CuZr sample had more like Cu^+ species. Grünert *et al.* [38] observed a reduction of Cu^{2+} species to Cu^+ under vacuum and X-ray irradiation in the case of Cu-ZSM-5 catalysts. Di Castro and Piredda [39] also observed very similar phenomenon in the case of catalysts that contained well dispersed CuO species that were supported on SiO_2. Thus, according to the literature reports, we could explain these experimental results in the following way: better Cu dispersion (in 10-CuZr) provides higher photoreduction of Cu^{2+}, due to the X-ray irradiation during

the XPS measurement [40]. The stabilization of Cu^{+} ions on the surface of the catalyst is mainly due to the strong support interfacial interaction with these Cu species [41]. Therefore, the low energy XPS peak observed at 932.2 eV could be assigned to Cu^{+} species which are interacted with ZrO_2. It is interesting to note that Moretti *et al.* [42] assigned lower BE values for interactive Cu species and they explained that the reason for that is the formation of more covalent Cu–O bond due to strong interaction between CuO and ZnO. These observations lead to the fact that CuO and ZrO_2 in CuZr samples are not a physical mixture, but a chemical interaction existed between them. Furthermore, the existence of two different Cu species is also consistent with the H_2-TPR results, where we observed two TPR peaks corresponding to two reducible species. The contribution of the area under the peak at 932.2 eV is higher for 10-CuZr than 20-CuZr sample, indicating that the amount of the interactive species is higher in the case of 10-CuZr than the 20-CuZr sample.

The Zr *3d* XP spectra for CuZr samples are shown in Figure 6C. A spin-orbit doublet was observed for Zr $3d_{5/2}$ and $3d_{3/2}$ core levels centered at 181.8 eV and 184.2 eV respectively. The BE value of *ca.* 181.8 eV measured for Zr $3d_{5/2}$ indicates the presence of ZrO_2 with an oxidation state of +4 [43]. It was also reported that the BE of Zr^{4+} species in pure ZrO_2 is around 182.6 eV [44]; slightly lower values were observed in case of CuZr samples compared to that of stoichiometric ZrO_2. This is probably due to oxygen deficiency. The shift in the BE toward the lower value might be associated with the holes created by oxygen vacancies in the ZrO_2 lattice [45].

The deconvoluted XP O *1s* spectra for CuZr samples (Figure 6D) show two peaks at 530 eV and 531.5 eV. Wu *et al.* [46] observed two types of oxygen species for the Cu-supported ZrO_2 catalysts: oxygen species of ZrO_2 and/or CuO and oxygen species of Zr–OH, whose binding energy is in the range of 529.8–530.3 eV and 530.9–532.2 eV, respectively. Navio *et al.* [47] also observed two types of oxygen species in the ZrO_2 sample: oxygen species of ZrO_2 and oxygen species of Zr–OH, whose binding energy is in the range of 529.8 to 530.3 and 530.9 to 532.2 eV, respectively. The three samples showed XPS peaks corresponding to oxygen species corresponding to ZrO_2 and/or CuO and oxygen species of Zr–OH in different proportions.

The degree of dispersion of Cu and Zr atoms on the surface of the catalysts, estimated from XPS results, are shown in Table 2. From these values, as expected, the surface of the 20-CuZr catalyst was enriched with Cu and Zr atoms compared with 10-CuZr sample. The bulk chemical composition of catalysts determined from ICP analysis (Table 2) clearly differs from the surface composition. The quantity of Cu on the surface of both the catalysts is less than in the bulk. This is most probably due to deposition of Cu species inside the mesopores of ZrO_2 support. A very similar behavior was observed in case Fe_2O_3 supported mesoporous ZrO_2 catalysts [20].

The acidic properties of bare ZrO_2 and porous CuO-ZrO_2 samples were evaluated using FTIR spectroscopy following pyridine adsorption and NH_3-TPD techniques. The results of the analysis are shown in Figure 7 and Table 3. The spectrum of bare ZrO_2 sample showed only a small peak corresponding to Brönsted acid sites. In contrast, the nanocomposite samples showed peaks due to Brönsted and Lewis acid sites. In comparison, 20-CuZr sample showed a lower number of Brönsted and Lewis acid sites than the 10-CuZr sample. The spectra of these two samples displayed well resolved bands at 1443, 1490 and 1545 cm^{-1}. It is well known that the band at 1443 cm^{-1} could be ascribed to Lewis-coordinated pyridine (L), whereas Brönsted coordinated pyridine (B) generally shows a band at 1545 cm^{-1}. Another band at 1490 cm^{-1} could be assigned to Lewis and Brönsted-coordinated pyridine (L + B) [48].

The 10-CuZr sample possessed dominant Lewis acid sites with a small number of Brönsted acid sites. As expected, 20-CuZr sample showed a similar trend as 10-CuZr sample; existence of higher number of Lewis acid sites than Brönsted acid sites. The concentration of the Brönsted (B) and Lewis (L) acid sites for each catalyst was determined by calculating the intensities of the FTIR bands corresponding to respective acid sites [49]. Quantitative data was obtained by using the Lambert-Beer equation [50] and the data is presented in Table 3. The results presented in Table 3 clearly indicate that

an increase of CuO loading to 20 wt. % resulted in a decrease of the both Brönsted and Lewis acid sites concentration.

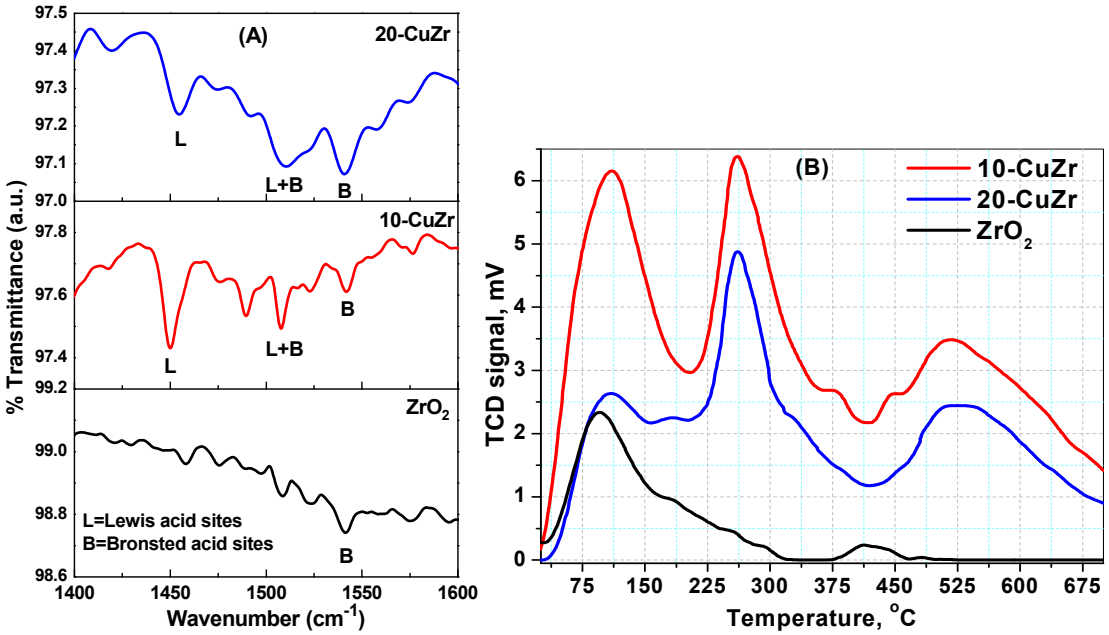

Figure 7. (**A**) FTIR spectra after pyridine adsorption (**B**) NH_3-TPD patterns for ZrO_2 and CuZr nanocomposite samples.

Table 3. Results from FTIR analysis of pyridine adsorption and NH_3-TPD measurements.

Catalyst	Number of Acid Sites [a] ($\mu mol \cdot g^{-1}$)		Number of Acid Sites [a] ($\mu mol \cdot g^{-1}$)	Amount of NH_3 Desorbed [b] ($mmol \cdot g^{-1}$)	Density of Acid Sites [b] ($mmol \cdot m^{-2}$)
	Brönsted (B)	Lewis (L)			
ZrO_2	0.7	0	0.0	0.25	0.023
10-CuZr	22.3	42.6	0.52	1.48	0.081
20-CuZr	14.4	20.8	0.69	1.12	0.062

[a] FTIR spectra after pyridine adsorption; [b] NH_3-TPD analysis.

The NH_3-TPD technique was used to investigate the strength and number of acidic sites presented in the samples. Figure 8B shows the NH_3-TPD profiles obtained for all the samples. The number of total acidic sites were measured from intensity of NH_3 desorption peaks and the density of total acidic sites of each catalyst was obtained by dividing the number of total acidic sites by surface area of the catalyst [51]. It is widely accepted that the NH_3 desorption temperature provides the information about the strength of acidic sites presented in the samples; desorption peaks appearing below 200 °C could be attributed to weak acidic sites and desorption peaks between 200 and 450 °C could be due to the presence of acidic sites with medium strength, while ammonia desorption peaks appearing at high temperatures (more than 450 °C) could be representative of strong acidic sites.

Synthesized ZrO_2 and CuZr samples showed desorption peaks in the temperature range of 40 to 700 °C, which is an indication that the samples possessed weak, medium and strong acid sites. All the samples showed broad desorption peak at low temperature in the range of 75–200 °C, whichcorresponds to weak acid sites. Desorption of NH_3 from weak acidic sites is known to be a result of hydrogen bonded NH_3 rather than desorption of ammonia from the acidic sites on the surface of the sample. On other hand, CuZr nanocomposite samples showed desorption peaks at 270 °C and 525 °C, which can be attributed to the medium and strong acid sites, respectively. Impregnation of CuO on ZrO_2 support resulted a notable increase in the number of acid sites. The 20-CuZr sample exhibited a

lower NH_3 desorption amount than 10-CuZr sample, as can be deduced by the comparison between the areas of desorption peaks for these two samples. These results clearly indicate the formation of a great number of acid sites in the CuZr nanocomposites. This is probably due to the effect of fine dispersion of CuO on the surface of ZrO_2 [52].

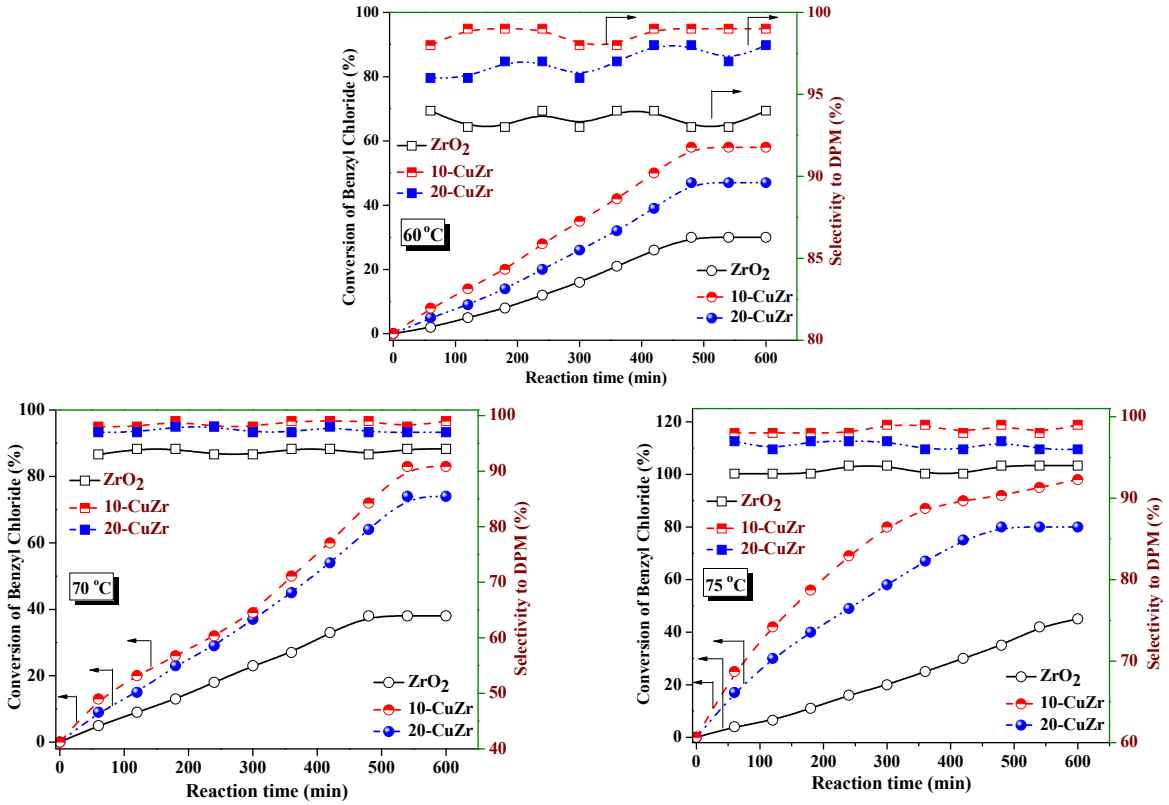

Figure 8. Benzyl chloride conversion levels and diphenylmethane (DPM) selectivities with reaction time over ZrO_2 support, CuZr catalysts at different reaction temperatures (benzne/benzyl chloride stoichiometric ratio = 15 and 0.1 g of catalyst).

The density of acidic sites for all the catalysts are presented in Table 3. Increase of CuO loading affected the total number of acidic sites of CuZr catalysts, particularly Lewis acid sites. It is reported in the literature [53] that monoclinic ZrO_2 has more acidic sites compared to tetragonal ZrO_2. In addition, enhancement of surface acidity was observed in case of Cu and Zr mixed oxide catalysts because of increase in number of oxygen deficient sites accompanied with the charge imbalance based on the generation of Cu–O–Zr interactive species [54]. XRD results clearly indicate that the 10-CuZr sample possessed more tetragonal ZrO_2 volume percent than the 20-CuZr sample.

The catalytic performance of ZrO_2 support and CuZr nanocomposite samples are tested for benzylation of benzene with benzyl chloride (Scheme 1). Benzylation of benzene (**1**) with benzyl chloride (**2**) as an alkylating agent produces mainly diphenylmethane (**3**). As the Friedel-Crafts reaction is always accompanied by di- and poly-alkylations, due to higher reactivity of the product than the reactant, the benzylation reaction could also give dibenzylation products (**4**–**6**) as side products. Thus, dibenzylbenzene, tribenzylbenzene, *etc.*, may be formed in the reaction,with dibenzylbenzene being the most prominent side product.

The conversion levels of benzyl chloride and selectivity to DPM values with reaction time over ZrO_2 and CuZr nanocomposite catalysts at different reaction temperatures are shown in Figure 8. As shown in Figure 8, bare ZrO_2 support showed only 45% of benzyl chloride conversion at 75 °C after 600 min. Benzylation activity improved significantly after 10 wt. % CuO loading on ZrO_2 support,

58% of benzyl chloride conversion was observed at 65 °C and it reached 98% at 75 °C after 600 min. Increase of CuO loading to 20 wt. % resulted in a decrease in conversion of benzyl chloride to 80% at 75 °C. With an increase of reaction temperature, the benzyl chloride conversion increased in the case of all of the catalysts.

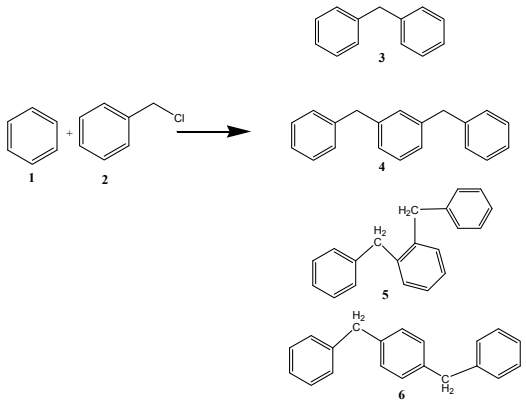

Scheme 1. Reaction scheme for benzylation of benzene.

The selectivity to DPM and rates of reaction per unit surface area of ZrO_2 support and CuZr nanocomposite at 65 °C, 70 °C and 75 °C are presented in Table 4. The 10-CuZr catalyst offered the highest benzylation rate, followed by 20-CuZr and then ZrO_2 support. All three catalysts showed more or less the same reaction rates per unit surface area at 65 °C and 70 °C; however, the major difference was observed at 75 °C, where the 10-CuZr catalyst showed higher reaction rates per unit surface area.

Table 4. Selectivity to diphenylmethane and reaction rate per unit surface area for ZrO_2 and CuZr nanocomposite catalysts at different reaction temperatures after 10 h of reaction.

Catalyst	65 °C		70 °C		75 °C	
	Selectivity (%)	$\bar{k}$ ($min^{-1} \cdot m^{-2} \cdot g$), 10^{-5}	Selectivity (%)	$\bar{k}$ ($min^{-1} \cdot m^{-2} \cdot g$), 10^{-5}	Selectivity (%)	$\bar{k}$ ($min^{-1} \cdot m^{-2} \cdot g$), 10^{-5}
ZrO_2	94	0.69	94	0.98	94	1.50
10-CuZr	99	2.27	99	4.18	99	5.79
20-CuZr	98	1.79	97	2.68	96	3.75

A clear difference was observed in benzylation activity of CuZr nanocomposites with different CuO composition; thus, it can be assumed that the catalytic activity of these catalysts in benzylation was affected by their composition and physico-chemical properties. The kinetic data for the benzylation reaction in excess of benzene (stoichiometric ratio of benzene/benzyl chloride = 15) over ZrO_2 support and CuZr nanocomposites could be fitted well to a pseudo-first-order rate law: $\ln[1/1 - x] = k[t - t_0]$ where k is the apparent first-order rate constant, x is the fractional conversion of benzyl chloride, t is the reaction time and t_0 is the induction period which corresponds to the time required for reaching equilibrium temperature. Plots of $\ln[1/1 - x]$ as a function of time at 65 °C, 70 °C and 75 °C were shown in Figure 9.

It is clear from the data tabulated in Table 4 that the reaction rate constant k_a for 10-CuZr catalyst is much higher than that of bare ZrO_2 support. In addition, the turnover frequency (TOF) was calculated based on the number of moles of benzyl chloride converted per moles of metal oxide per second. The observed TOF is 97.8 h^{-1} for ZrO_2, 1234.5 h^{-1} for 10-CuZr and 983.1 h^{-1} for 20-CuZr, respectively (supporting information, Table S1). The TOF data again reveal that the enhancement of catalytic performance was influenced by the CuO loading. The influence of TOF on the CuO loading clearly suggests that the presence of a higher number of CuO-ZrO_2 interactive species plays a role in benzylation activity. The DPM selectivity is more or less the same in the case of ZrO_2 and CuZr

nanocomposites. The product distribution mainly comprised of DPM (99%), with a minor quantity of DBE (6%).

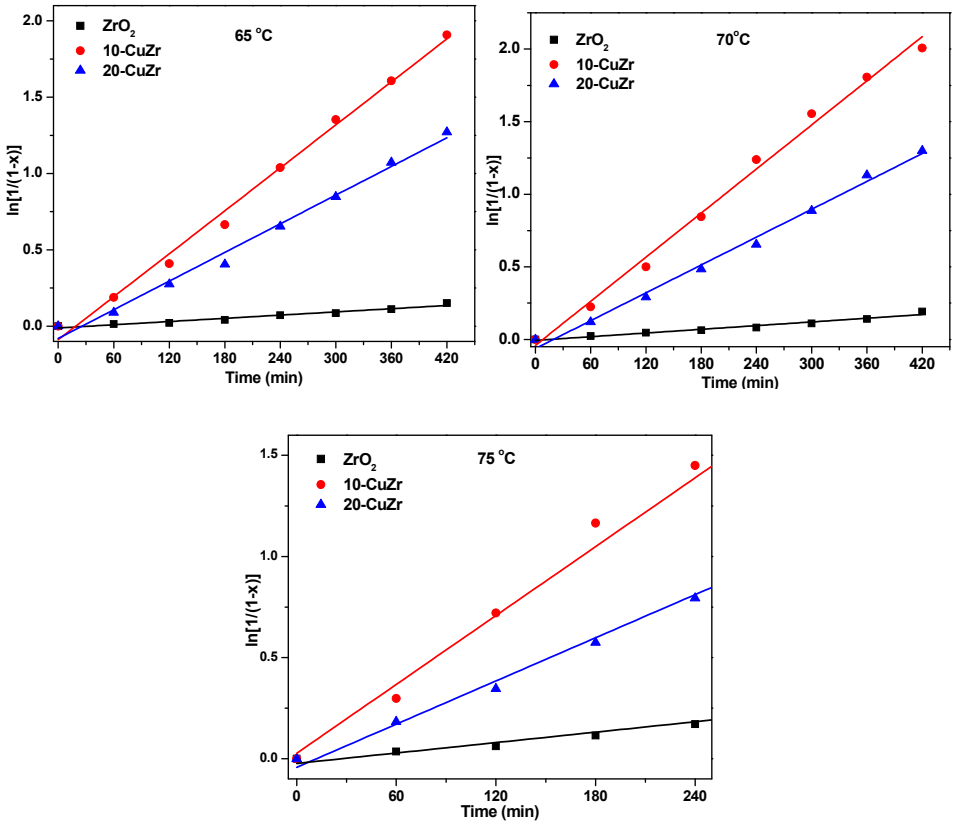

Figure 9. Plot of $\ln[1/(1-x)]$ as a function of the reaction time for all catalysts.

It is widely reported that the crucial step in the Friedel-Crafts alkylation mechanism is the formation of the carbocation and the acidic centers presented in the catalyst facilitates the carbocation formation [13]. The synthesized CuZr catalysts possessed mainly Lewis and Brönsted acid centers, which are primarily responsible for catalyzing the selective benzylation. A significant increase of activity after impregnation of 10 wt. % CuO over ZrO_2 was clearly observed and further increase of CuO loading to 20 wt. % resulted decrease catalytic activity. The decrease of activity is primarily related to the fact that 20-CuZr sample possessed crystalline CuO species and a lower number of CuO-ZrO_2 interactive species.

To obtain an insight into the role of CuO loading in the benzylation reaction, we determined the activation energy (E_a) for benzylation of benzene over CuZr nanocomposites. The Arrhenius equation was used to calculate the benzylation reaction rate constant (k_a) for three catalysts at 65 °C, 70 °C and 75 °C. The Arrhenius plots of benzylation reaction for ZrO_2 support and CuZr nanocomposite samples are shown in Figure S3 (supporting information). The calculated E_a values are shown in Table S1. The apparent activation energy for ZrO_2 support, 10-CuZr and 20-CuZr is 65.9 kJ·mol^{-1}, 59.2 kJ·mol^{-1} and 62.3 kJ·mol^{-1}, respectively, and the observed values are in relatively good accordance with the benzylation activity shown by these samples.

The XRD, DR UV-vis, XPS and H_2-TPR characterization results reveal that CuZr samples are not simply a physical mixture. Instead, a strong interaction exists between CuO and ZrO_2, which led to the formaction of Cu^{2+}–O–Zr^{4+} bonds in these samples. The XRD pattern of 10-CuZr sample did not show presence of Cu_2O or CuO crystalline phase, which means Cu^+ and Cu^{2+} species should have presented as highly disperse phases on the surface of the ZrO_2, probably due to strong interaction of CuO with ZrO_2 at 10 wt. % CuO loading. It has been reported that Cu^{2+} ions can be incorporated

into the ZrO_2 lattice; however, incorporation of Cu did not occur, since no mixed oxide phase was observed in the CuZr samples. XPS spectra of CuZr samples clearly showed two different peaks corresponding to two different surface Cu species with different oxidation states (Cu^{2+} and Cu^{+}). It is most probable that the Cu ions are bonded to the oxygen anions on the surface of ZrO_2 forming Zr–O–Cu groups. It was also reported that the formation of the Cu–O–Zr bonds in CuAlZr containing catalysts brings a synergistic interaction between Cu and Zr and this facilitates the reduction of Cu^{2+} species [55]. An enhanced reducibility of Cu^{2+} in both of the. CuZr samples observed by H_2-TPR results provide strong evidence that Cu–O–Zr bonds presented in the synthesized samples. Dongare *et al.* [23] observed a decrease of lattice parameters of ZrO_2 with an increase of Cu content (maximum 20 mol%). The authors claimed that incorporation of Cu^{2+} in the lattice position of Zr^{4+} ions could be the main reason for this. Hu *et al.* [55] also observed that addition of CuO delayed the phase transformation of ZrO_2 from tetragonal to monoclinic at 700 °C. These authors observed a decrease in lattice parameter of ZrO_2 with an increase of CuO content to 30 mol%. We also calculated the lattice parameters of all the catalysts (Table S2) and have not observed any considerable change after 10 wt. % or 20 wt. % of CuO impregnation. This is possibly due to the different method of preparation we adopted to synthesize the CuZr catalysts in this study. The characterization results also clearly indicated that the CuO particles were dispersed on bulk ZrO_2 structure. It is known that, upon thermal treatment, CuO particles could sinter and agglomerate readily. The sintering and agglomeration was more pronounced in the case of 20-CuZr sample. In contrast, highly dispersed CuO species were formed in the case of 10-CuZr catalyst. Formation of highly dispersed CuO species in the case of 10-CuZr sample is responsible for improved catalytic performance.

It is well known that Friedel-Crafts alkylation is an electrophilic substitution reaction in which complexation of alkyl or aryl halide with the catalyst lead to formation the carbocation [56]. Then, the formed carbocation attacks the aromatic species to form mono-alkylation product and hence formation of carbocation is a crucial step in the reaction mechanism. Thus, a catalyst which contained strong Lewis acid sites could produce carbocation efficiently to offer an enhanced activity in benzylation of benzene with benzyl chloride. The NH_3-TPD and FTIR pyridine adsorption measurements revealed that 10-CuZr catalyst possessed mostly strong Brönsted and Lewis acid sites and showed the highest benzylation activity. The different spacing and symmetry of the Zr–O and –OH bonds at tetragonal ZrO_2 phase (20-CuZr) and monoclinic ZrO_2 (10-CuZr) could also play a key role in determining the dispersion of the active metal component and the catalytic properties of Cu-Zr catalysts [57].

We are interested in comparing the activity of the CuZr nanocomposites with the reported Cu based catalysts. In comparison with the Cu-exchanged clay [18] and Cu-HMS [19] catalysts, 10-CuZr catalyst is more active and equally stable at very similar conditions. The previously reported mesoporous Cu catalysts (Cu-clay and Cu-HMS) showed 100% conversion with good selectivity to mono-alkyl product at 80 °C; however, 10-CuZr catalyst synthesized in this study offered the same activity at low reaction temperature (75 °C), indicating that 10-CuZr is more active than Cu-clay and Cu-HMS catalysts.

3. Reusability of CuZr Nanocomposite Catalysts

It is a known fact that reusability is one of the main advantages of heterogeneous catalysts over homogenous catalysts. The most active catalyst, 10-CuZr catalyst, was used to test the reusability of CuZr nanocomposites. The reaction was performed at 75 °C, using same conditions as described in the experimental section. The conversion levels of benzyl chloride of this catalyst for six consecutive reaction cycles were determined. The fresh catalyst showed 98% conversion after 600 min. The first and second cycles of reused catalysts offered exactly the same conversion levels. A slight decrease of conversion level (94%) was observed in fourth, fifth and sixth cycles. The decrease in conversion levels in the later cycles could be due to loss of catalyst during the filtration of catalyst after completion of the cycle. The observed results indicate that the catalyst could be recycled several times without losing activity.

4. Experimental Section

4.1. Reagents

All the purchased analytical grade reagents were used as received without any treatments. Zirconyl chloride octahydrate [($ZrOCl_2 \cdot 8H_2O$)], cupric nitrate trihydrate [$Cu(NO_3)_2 \cdot 3H_2O$], aqueous ammonia solution and tetrabutyl ammonium bromide [$(CH_3CH_2CH_2CH_2)_4N(Br)$], benzene [$C_6H_6$] and benzyl chloride [$C_6H_7Cl$] were purchased from Aldrich, Dorset, UK.

4.2. Synthesis of Nanosized Porous CuO-ZrO_2 Materials

Tetrabutyl ammonium bromide was used as templating agent to synthesize nanocrystalline porous ZrO_2 support by a simple sol-gel method. The typical synthesis method is as follows: the calculated amount of $ZrOCl_2 \cdot 8H_2O$ (26.1 g) was dissolved in 100 mL of distilled water. To this solution, 100 mL of 0.88 mol tetrabutyl ammonium bromide solution was added under constant stirring. The temperature of the solution was maintained at 50 °C in a water bath and then subjected to ultrasonication for 5 h. Then the solution was aged at 80 °C for four days to obtain a gel. The obtained gel was then washed with ethanol five times and dried at 100 °C for 24 h. Bare ZrO_2 support was obtained by calcination of dried powder at 500 °C in a Muffle furnace for 3 h. The calcined material was labelled as ZrO_2.

CuO supported ZrO_2 nanocomposites were prepared by a simple impregnation method. The calculated amount of $Cu(NO_3)_2 \cdot 3H_2O$, which corresponded to 10.0 wt. % and 20.0 wt. % of CuO, was dissolved in distilled water, and the calculated amount of dried ZrO_2 powder was added to cupric nitrate solution under continuous stirring. The excess water was removed by drying the contents at 100 °C in an electric oven. A portion of the prepared CuO-ZrO_2 material was thermally treated at 500 °C in a Muffle furnace and kept at this temperature for 3 h. The calcined materials were labelled using the following nomenclature: 10-CuZr and 20-CuZr, for 10 wt. % and 20 wt. % CuO supported ZrO_2 samples respectively.

4.3. Characterization of Catalysts

The elemental composition of the synthesized materials was determined by using ICP-AES, Optima 7300DV (Perkin Elmmer Corporation, Waltham, MA, USA) instrument. The sample preparation for elemental analysis was carried out as follows: approximately 100 mg of material was placed in a Teflon beaker and the material was dissolved in a mixture of acids (10 mL of 40% HF, 4 mL of HNO_3 and 4 mL HCl) and then 20 mL of deionized H_2O was added to the solution. The solution was then kept in an ultrasonic bath for 10 min to obtain homogeneous dissolution. Then, the solution was transferred into a centrifuge tube and centrifuged at 3000 rpm for five minutes. The clear supernatant solution was decanted and used to prepare 250 mL stock solution.

Powder X-ray diffraction (XRD) measurements were carried out using a Bruker diffractometer (Bruker D8 advance target) (Bruker, Karlsruhe, Germany). The patterns were obtained using Cu $K\alpha_1$ and a monochromator (λ = 1.5405Å) at 40 kV and 40 mA. The crystallite size of the ZrO_2 phase was calculated using Scherrer Equation (3):

$$D = B\lambda/\beta_{1/2}\cos\theta \quad (3)$$

where D is the average crystallite size of the phase under investigation, B is the Scherrer constant (0.89), λ is wavelength of the X-ray beam used (1.5405 Å), $\beta_{1/2}$ is the full width at half maximum (FWHM) of the diffraction peak and θ is the diffraction angle. The identification of different crystalline phases in the samples was performed by comparing the data with the Joint Committee for Powder Diffraction Standards (JCPDS) files. A Bruker Equinox 55 FT-IR spectrometer equipped with an FRA106/S FT Raman module and a liquid N_2 cooled Ge detector using the 1064 nm line of a Nd:YAG laser with an output laser power of 200 mW was used to obtain Raman spectra for the synthesized samples. Diffuse reflectance UV-vis (DRUV-vis) spectra for all the samples were collected using a Thermo-Scientific

evolution 600 UV-vis spectrophotometer combined with an integrating sphere in the wavelength range of 200–800 nm to measure the reflectance spectra of a sample. A small amount of the sample in powder form was dispersed and pressed firmly between two microscope glass plates to create a thin absorbing film.

Scanning Electron Microscopy (SEM) measurements were carried out using a JEOL JSM840A instrument (JEOL, Tokyo, Japan). For measurements, the powder sample was attached to an aluminum block using double sided carbon tape. The textural properties of the synthesized samples were determined from the N_2 physisorption measurements at −196 °C using a NOVA 3200e automated gas sorption system (Quantachrome, Boynton Beach, FL, USA). Prior to measurement, the sample was outgassed for 6 h at 150 °C. The specific surface area was determined by using the Brunauer-Emmett-Teller (BET) equation. The average pore radius was estimated from the relation $2Vp/S_{BET}$, where Vp is the total pore volume (at $P/P^0 = 0.975$). Pore size distribution patterns were generated by the Barrett-Joyner-Halenda (BJH) analysis of the desorption branches, and the values for the average pore radius were calculated. The X-ray photoelectron spectroscopy (XPS) measurements for all the samples were carried out using a SPECS GmbH XPS spectrometer (SPECS, Berlin, Germany). Prior to analysis, the samples were outgassed under vacuum inside the load lock for 16 h. The binding energy (BE) of the adventitious carbon (C *1s*) line at 284.6 eV was used for calibration, and the positions of other peaks were corrected according to the position of the C *1s* signal. For the measurements of high resolution spectra, the analyzer was set to the large area lens mode with energy steps of 25 m eV and in Fixed Analyzer Transmission (FAT) mode with pass energies of 34 eV and dwell times of 100 ms. The XPS spectra of the materials were recorded with the acceptance area and angle of 5 mm in diameter and up to $\pm 5^{\circ}$, respectively. The base pressure during all measurements was 5×10^{-9} mbar. A standard dual anode excitation source with Mg Kα (1253.6 eV) radiation was used at 13 kV and 100 W.

Perkin-Elmer Spectrum 100 FTIR spectrometer was used to obtain DRIFT spectra of calcined materials. Then, DRIFT measurements for the samples after pyridine adsorption was carried out using the same instrument. The analysis was performed over a calculated amount of catalyst which was treated at 100 °C under vacuum for 5 h. Then, the sample was treated with pyridine vapor and finally heated at 100 °C under vacuum for 30 min to remove physically adsorbed pyridine. DRIFT spectra were collected at room temperature. The number of Brönsted (B) and Lewis (L) acid sites presented in the sample was determined via integration of the area of the absorption bands showing the maximum values of intensity at 1443 and 1545 cm^{-1}, respectively. A blank spectrum of catalyst sample was recorded before pyridine adsorption and hence it is subtracted before the calculations of Brönsted and Lewis concentration. Integrated absorbance of each band was obtained using the software by applying the corresponding extinction coefficient and normalized by the weight of the samples used for the analysis.

Ammonia temperature programmed desorption (NH_3-TPD) measurements were performed to titrate the total number of acid sites, using CHEMBET-3000 (Quantachrome, Boynton Beach, FL, USA) equipped with TCD detector, PID-controlled furnace heated flow micro-reactor. Calculated amount of catalyst sample (250 mg) was pretreated at 120 °C for 2 h under helium gas flow (80 $mL \cdot min^{-1}$). The gas flow was switched to ammonia to saturate the sample for 1 h and then the sample flushed by flowing helium gas at 100 °C for 2 h to remove physisorbed ammonia prior to recording the TCD signal. The NH_3 desorption patterns were recorded by ramping the temperature of the sample to 800 °C at a rate of 10 °C min^{-1} under a steady flow (80 $mL \cdot min^{-1}$) of helium gas. The amount of ammonia evolved was determined by comparing the areas desorbed from the sample with those of known amounts of injected ammonia.

H_2-Temperature programmed reduction (H_2-TPR) experiments were carried out using CHEMBET-3000 instrument (Quantachrome, Boynton Beach, FL, USA). Approximately 80 mg of catalyst was loaded into a quartz tube and the sample treated with 10% oxygen + 90% helium gas mixture at 120 °C for 30 min, and then the gas flow was switched to helium gas to flush the sample. Then, the sample temperature was brought down to 25 °C and the flow of the gas was changed to

5% hydrogen + 95% helium gas mixture. Finally, the TCD signal was recorded by raising the sample temperature to 600 °C at the rate of 5 °C min^{-1} to obtain the H_2-TPR pattern of a sample.

4.4. Benzylation of Benzene Using Benzyl Chloride

A three necked round-bottomed glass flask equipped with a reflux condenser was used to carry out the liquid phase benzylation of benzene with benzyl chloride (BC) under atmospheric pressure. The temperature of the reaction was monitored and electrically heated in a precisely controlled oil bath. In a typical run, 0.1 g of activated catalyst was transferred into a round bottom flask, which contained 15 mL of benzene. Then, the temperature of the flask was increased to the required reaction temperature and then 1 mL of BC was added to flask to start the reaction and the moment BC added was regarded as the initial reaction time. Liquid samples were withdrawn at regular intervals and analyzed by gas chromatography (HP-6890) equipped with an FID detector and HP-5 capillary column. The products were also identified by GC-MS (HP-5975C) analysis. Because the benzene was in excess, the performance of the catalyst was determined based on the conversion of the benzylating reagent, *i.e.*, BC. The conversion of BC selectivity to the major product diphenylmethane (DPM) and other minor products, turnover number (TON) and turnover frequency (TOF) of catalysts were measured by using the following equations.

$$\text{Conversion of BC} = \frac{\text{The amount of BC converted/min}}{\text{The amount of BC fed/min}} \times 100 \quad (4)$$

$$\text{Selectivity of DPM} = \frac{\text{The amount of DPM obtained}}{\text{The amount of total products}} \times 100 \quad (5)$$

$$\text{Turnover number (TON)} = \frac{\text{Moles of product formed}}{\text{Moles of CuO} - \text{ZrO2 catalyst}} \quad (6)$$

$$\text{Turnover frequency (TOF)} = \frac{\text{TON}}{\text{Time of reaction}} \quad (7)$$

5. Conclusions

Mesoporous CuO-ZrO_2 catalysts were successfully synthesized by adopting modified sol-gel method using tetrabutyl ammonium bromide as a templating agent. Bare ZrO_2 support was composed of mixture of tetragonal and monoclinic ZrO_2 phases; however, the ZrO_2 phase was mostly transformed into tetragonal after impregnation of 20 wt. % CuO. The XPS results evidently indicated that 10-CuZr sample possessed more interactive species than 20-CuZr sample. Preferential formation of interactive species on the surface of ZrO_2 support and the dispersion of the Cu^{2+} species depended on the CuO loading. H_2-TPR results suggested that these Cu^{2+} species strongly interacted with ZrO_2, resulting in the formation of easily reducible Cu^{2+}–O–Zr^{4+} bonds. On other hand, the 20-CuZr sample showed formation crystalline CuO particles on the ZrO_2 surface. The 10-CuZr catalyst offered higher catalytic activity than 20-CuZr in benzylation of benzene under identical reaction conditions. The superior catalytic activity of 10-CuZr catalyst is attributed to possession of more CuO-ZrO_2 interactive species and a mesoporous structure, which provided larger active sites with easy reducibility and accessible strong Brönsted and Lewis acid sites.

Supplementary Materials: Figure S1: Raman spectra of the samples, Figure S2: EDX spectra of (**a**) ZrO_2 (**b**) 10-CuZr and (**c**) 20-CuZr samples, Figure S3: Arrhenius plots of benzylation reaction for all the catalysts, Table S1: Activation energies (*Ea*), TON and TOF for the catalytic reaction conducted over different catalysts, Table S2: Crystal Lattice parameters measured from XRD analysis.

Acknowledgments: This project was funded by the National Plan for Science, Technology and Innovation (MAARIFAH)-King Abdulaziz City for Science and Technology-the Kingdom of Saudi Arabia-award number (11-NAN 2057-03). The authors also, acknowledge with thanks Science and Technology Unit, King Abdulaziz University for technical support.

Author Contributions: S.N.B. and M.M. conceived and designed the experiments; E.H.A., T.T.A., H.A.M. and K.N. performed all experiments and characterization tests as well as share in analysis of the data. Both T.T.A. and K.N. wrote the paper, share in data analysis and revised the manuscript; M.M. and T.T.A. proofread the manuscript.

Conflicts of Interest: The authors declare no conflict of interest.

References

1. Tanabe, K. Surface and catalytic properties of ZrO_2. *Mater. Chem. Phys.* **1985**, *13*, 347–364. [CrossRef]
2. Tsoncheva, T.; Genova, I.; Dimitrov, M.; Sarcadi-Priboczki, E.; Venezia, A.M.; Kovacheva, D.; Scotti, N.; dal Santo, V. Nanostructured copper-zirconia composites as catalysts for methanol decomposition. *Appl. Catal. B* **2015**, *165*, 599–610. [CrossRef]
3. Rhodes, M.D.; Pokrovski, K.A.; Bell, A.T. The effects of zirconia morphology on methanol synthesis from CO and H_2 over Cu/ZrO_2 Implication of the role of oxygen anions catalysts (Part II). Transient-response infrared studies. *J. Catal.* **2005**, *233*, 210–220. [CrossRef]
4. Wang, L.C.; Liu, Q.; Chen, M.; Liu, Y.M.; Cao, Y.; He, H.Y.; Fan, K.N. Structural evolution and catalytic properties of nanostructured Cu/ZrO_2 catalysts: Prepared by oxalate Gel-Coprecipitation technique. *J. Phys. Chem. C* **2007**, *111*, 16549–16557. [CrossRef]
5. Ma, Z.Y.; Yang, C.; Wei, W.; Li, W.H.; Sun, Y.H. Catalytic performance of copper supported on zirconia polymorphs for CO hydrogenation. *J. Mol. Catal. A* **2005**, *231*, 75–81. [CrossRef]
6. Inui, K.; Kurabayashi, T.; Sato, S. Direct synthesis of ethyl acetate from ethanol carried out under pressure. *J. Catal.* **2002**, *212*, 207–215. [CrossRef]
7. Mayr, L.; Klotzer, B.; Zemlyanov, D.; Penner, S. Steering of methanol reforming selectivity by zirconia-copper interaction. *J. Catal.* **2015**, *321*, 123–132. [CrossRef]
8. Luo, J.; Xu, H.; Liu, Y.; Chu, W.; Jiang, C.; Zhao, X.A. facile approach for the preparation of biomorphic $CuO\text{-}ZrO_2$ catalyst for catalytic combustion of methane. *Appl. Catal. A* **2012**, *423–424*, 121–129. [CrossRef]
9. Gaspar, A.B.; Esteves, A.M.L.; Mendes, F.M.T.; Barbosa, F.G.; Appel, L.G. Chemicals from ethanol- the ethyl acetate one-pot synthesis. *Appl. Catal. A* **2009**, *363*, 109–114. [CrossRef]
10. Gaspar, A.B.; Barbosa, F.G.; Letichevsky, S.; Appel, L.G. The one-pot ethyl acetate synthesis: The role of the support in the oxidative and the dehydrogenative routes. *Appl. Catal. A* **2010**, *380*, 113–117. [CrossRef]
11. Qu, F.F.; Chu, W.; Shi, L.M.; Chen, M.H.; Hu, J.Y. Catalytic combustion of methane over nano ZrO_2-supported copper-based catalysts. *Chin. Chem. Lett.* **2007**, *18*, 993–996. [CrossRef]
12. Baeza, B.B.; Ramos, I.R.; Guerrero-Ruiz, A. Interaction of Carbon Dioxide with the Surface of Zirconia Polymorphs. *Langmuir* **1998**, *14*, 3556–3564. [CrossRef]
13. Coq, B.; Gourves, V.; Figueras, F. Benzylation of toluene by benzyl chloride over protonic zeolites. *Appl. Catal.* **1993**, *100*, 69–75. [CrossRef]
14. Bachari, K.; Millet, J.M.M.; Benaichouba, B.; Cherifi, O.; Figueras, F. Benzylation of benzene by benzyl chloride over iron mesoporous molecular sieve materials. *J. Catal.* **2004**, *221*, 55–61. [CrossRef]
15. Brown, C.M.; Barlow, S.J.; McQuarrie, D.J.; Clark, J.H.; Kybett, A.P. Catalysts comprising metal compounds supported on a clay or hydrous silicate and their use. EP0352878, 31 January 1990.
16. Laszlo, P.; Mathy, A. Catalysis of Friedel-Crafts alkylation by a montmorillonite doped with transition metal cations. *Helv. Chim. Acta* **1987**, *70*, 577–586. [CrossRef]
17. Leng, K.; Sun, S.; Wang, B.; Sun, L.; Xu, W.; Sun, Y. Benzylation of benzene with benzyl chloride on iron-containing mesoporous mordenite. *Catal. Commun.* **2012**, *28*, 64–68. [CrossRef]
18. Cseri, T.; Bekassy, S.; Figueras, F.; Rizner, S. Benzylation of aromatics on ion-exchanged clays. *J. Mol. Catal. A* **1995**, *98*, 101–107. [CrossRef]
19. Bachari, K.; Cherifi, O. Benzylation of benzene and other aromatics by benzyl chloride over copper-mesoporous molecular sieves materials. *Catal. Commun.* **2006**, *7*, 926–930. [CrossRef]
20. Ali, T.T.; Narasimharao, K.; Ahmed, N.S.; Basahel, S.N.; Al-Thabaiti, S.; Mokhtar, M. Nanosized iron and nickel oxide zirconia supported catalysts for benzylation of benzene: Role of metal oxide support interaction. *Appl. Catal. A* **2014**, *486*, 19–31. [CrossRef]
21. On, D.T.; Nguyen, S.V.; Kaliaguine, S. New SO_2 resistant mesoporous La-Co-Zr mixed oxide catalysts for hydrocarbon oxidation. *Phys. Chem. Chem. Phys.* **2003**, *5*, 2724–2729.

22. Mokhtar, M.; Basahel, S.N.; Ali, T.T. Effect of synthesis methods for mesoporous zirconia on its structural and textural properties. *J. Mater. Sci.* **2013**, *48*, 2705–2713. [CrossRef]
23. Dongare, M.K.; Ramaswamy, V.; Gopinath, C.S.; Ramaswamy, A.V.; Scheurell, S.; Brueckner, M.; Kemnitz, E. Oxidation activity and ^{18}O-isotope exchange behavior of Cu-stabilized cubic zirconia. *J. Catal.* **2001**, *199*, 209–216. [CrossRef]
24. Yamamoto, T.; Tanaka, T.; Takenaka, S.; Yoshida, S.; Onari, T.; Takahashi, Y.; Kosaka, T.; Hasegawa, S.; Kudo, M. Structural analysis of iron and manganese species in iron- and manganese-promoted sulfated zirconia. *J. Phys. Chem. B* **1999**, *103*, 2385–2393. [CrossRef]
25. Mercera, P.D.L.; van Ommen, J.G.; Doesburg, E.B.M.; Burggraaf, A.J.; Ross, J.R.H. Zirconia as a support for catalysts: Evolution of the texture and structure on calcination in air. *Appl. Catal.* **1990**, *57*, 127–148. [CrossRef]
26. Goldstein, H.F.; Kim, D.; Yu, P.Y.; Bourne, L.C.; Chaminade, J.P.; Nganga, L. Raman study of CuO single crystals. *Phys. Rev. B* **1990**, *41*, 7192–7194. [CrossRef]
27. Xu, J.F.; Ji, W.; Shen, Z.X. Raman spectra of CuO nanocrystals. *J. Raman. Spectrosc.* **1999**, *30*, 413–415. [CrossRef]
28. Sahu, H.R.; Rao, G.R. XRD and UV-Vis diffuse reflectance analysis of CeO_2-ZrO_2 solid solutions synthesized by combustion method. *Proc. Indian Acad. Sci. Chem. Sci.* **2001**, *113*, 651–658.
29. Kong, A.; Wang, H.W.; Yang, X.; Hou, Y.W.; Shan, Y.K. A facile direct route to synthesize large-pore mesoporous silica incorporating high CuO loading with special catalytic property. *Microporous Mesoporous Mater.* **2009**, *118*, 348–353. [CrossRef]
30. Chary, K.V.; Sagar, G.V.; Srikanth, C.S.; Rao, V.V. Characterization and catalytic functionalities of copper oxide catalysts supported on zirconia. *J. Phys. Chem. B* **2007**, *111*, 543–550. [CrossRef] [PubMed]
31. Arena, F.; Italiano, G.; Barbera, K.; Bordiga, S.; Bonura, G.; Spadaro, L.; Frusteri, F. Solid-state interactions, adsorption sites and functionality of Cu-ZnO/ZrO_2 catalysts in the CO_2 hydrogenation to CH_3OH. *Appl. Catal. A* **2008**, *350*, 16–23. [CrossRef]
32. Sato, A.G.; Volanti, D.P.; Meira, D.M.; Damyanova, S.; Longo, E.; Bueno, J.M.C. Effect of the ZrO_2 phase on the structure and behavior of supported Cu catalysts for ethanol conversion. *J. Catal.* **2013**, *307*, 1–17. [CrossRef]
33. Liu, Z.; Amiridis, M.D.; Chen, Y. Characterization of CuO supported on tetragonal ZrO_2 catalysts for N_2O decomposition to N_2. *J. Phys. Chem. B* **2005**, *109*, 1251–1255. [CrossRef] [PubMed]
34. Velu, S.; Suzuki, K.; Gopinath, C.S.; Yoshida, H.; Hattori, T. XPS, XANES and EXAFS investigations of CuO/ZnO/Al_2O_3/ZrO_2 mixed oxide catalysts. *Phys. Chem. Chem. Phys.* **2002**, *4*, 1990–1999. [CrossRef]
35. Patela, A.; Shukla, P.; Rufford, T.; Wang, S.; Chena, J.; Rudolph, V.; Zhu, Z. Catalytic reduction of NO by CO over copper-oxide supported mesoporous silica. *Appl. Catal. A* **2011**, *409–410*, 55–65. [CrossRef]
36. Diaz-Droguett, D.E.; Espinoza, R.; Fuenzalida, V.M. Copper nanoparticles grown under hydrogen: Study of the surface oxide. *Appl. Surf. Sci.* **2011**, *257*, 4597–4602. [CrossRef]
37. Espinos, J.P.; Morales, J.; Barranco, A.; Caballero, A.; Holgado, J.P.; Gonzalez-Elipe, A.R. Interface Effects for Cu, CuO, and Cu_2O Deposited on SiO_2 and ZrO_2. XPS Determination of the Valence State of Copper in Cu/SiO_2 and Cu/ZrO_2 Catalysts. *J. Phys. Chem. B* **2002**, *106*, 6921–6929. [CrossRef]
38. Grünert, W.; Hayes, N.W.; Joyner, R.W.; Shpiro, E.S.; Siddiqui, N.R.H.; Baeva, G.N. Structure, Chemistry, and Activity of Cu-ZSM-5 Catalysts for the Selective Reduction of NO*x* in the Presence of Oxygen. *J. Phys. Chem.* **1994**, *98*, 10832–10846. [CrossRef]
39. Di Castro, V.; Piredda, G. Photoinduced reduction of silica supported CuO during XPS irradiation. *Chem. Phys. Lett.* **1985**, *114*, 109–113. [CrossRef]
40. Menon, U.; Poelman, H.; Bliznuk, V.; Galvita, V.V.; Poelman, D.; Marin, G.B. Nature of the active sites for the total oxidation of toluene by CuO-CeO_2/Al_2O_3. *J. Catal.* **2012**, *295*, 91–103. [CrossRef]
41. Martínez-Arias, A.; Fernández García, M.; Soria, J.; Conesa, J.C. Spectroscopic Study of a Cu/CeO_2 Catalyst Subjected to Redox Treatments in Carbon Monoxide and Oxygen. *J. Catal.* **1999**, *182*, 367–377. [CrossRef]
42. Moretti, G.; Fierro, G.; Jacono, M.L.; Porta, P. Characterization of CuO-ZnO catalysts by X-ray photoelectron spectroscopy: Precursors, calcined and reduced samples. *Surf. Interface Anal.* **1989**, *14*, 325–336. [CrossRef]
43. Słoczyński, J.; Grabowski, R.; Kozłowska, A.; Olszewski, P.; Lachowska, M.; Skrzypek, J.; Stoch, J. Effect of Mg and Mn oxide additions on the structural and adsorptive properties of Cu/ZnO/ZrO catalysts for the methanol synthesis from CO_2. *Appl. Catal. A* **2003**, *249*, 129–138. [CrossRef]

44. Wandelt, K. Photoemission studies of absorbed oxygen and oxide layers. *Surf. Sci. Rep.* **1982**, *2*, 1–12. [CrossRef]
45. Dongare, M.K.; Dongare, A.M.; Tare, V.B.; Kemnitz, E. Synthesis and characterization of copper-stabilized zirconia as an anode material for SOFC. *Solid State Ion.* **2002**, *455*, 152–153. [CrossRef]
46. Wu, G.S.; Wang, L.C.; Liu, Y.M.; Cao, Y.; Dai, W.L.; He, H.Y.; Fan, K.N. Implication of the role of oxygen anions and oxygen vacancies for methanol decomposition over zirconia supported copper catalysts. *Appl. Surf. Sci.* **2006**, *253*, 974–982. [CrossRef]
47. Navio, J.A.; Hidalgo, M.C.; Colon, G.; Botta, S.G.; Litter, M.I. Preparation and physicochemical properties of ZrO_2 and Fe/ZrO_2 prepared by a Sol-Gel technique. *Langmuir* **2001**, *17*, 202–210. [CrossRef]
48. Narasimharao, K.; Ali, T.T. Catalytic oxidative cracking of propane over nanosized gold supported $Ce_{0.5}Zr_{0.5}O_2$ catalysts. *Catal. Lett.* **2013**, *143*, 1074–1084. [CrossRef]
49. Purova, R.; Narasimharao, K.; Ahmed, N.S.I.; Al-Thabaiti, S.; Al-Shehri, A.; Mokhtar, M.; Schwieger, W. Pillared HMCM-36 zeolite catalyst for biodiesel production by esterification of palmitic acid. *J. Mol. Catal. A* **2015**, *406*, 159–167. [CrossRef]
50. Jehng, J.M.; Turek, A.M.; Wachs, I.E. Surface modified niobium oxide catalyst: synthesis, characterization, and catalysis. *Appl. Catal.* **1992**, *83*, 179–200. [CrossRef]
51. Delannay, F. *Characterization of Heterogeneous Catalysts*; Marcel Dekker: New York, NY, USA, 1984.
52. Kim, T.; Burrows, A.; Kiely, C.J.; Wachs, I.E. Molecular/electronic structure surface acidity relationships of model-supported tungsten oxide catalysts. *J. Catal.* **2007**, *246*, 370–381. [CrossRef]
53. Li, N.; Tompsett, G.A.; Zhang, T.; Shi, J.; Wyman, C.E.; Huber, G.W. Renewable gasoline from aqueous phase hydrodeoxygenation of aqueous sugar solutions prepared by hydrolysis of maple wood. *Green Chem.* **2011**, *13*, 91–101. [CrossRef]
54. Ma, Z.Y.; Yang, C.; Wei, W.; Li, W.H.; Sun, Y.H. Surface properties and CO adsorption on zirconia polymorphs. *J. Mol. Catal. A Chem.* **2005**, *227*, 119–124. [CrossRef]
55. Hu, Y.H.; Dong, L.; Shen, M.M.; Liu, D.; Wang, J.; Ding, W.P.; Chen, Y. Influence of supports on the activities of copper oxide species in the low-temperature NO + CO reaction. *Appl. Catal. B* **2001**, *31*, 61–69. [CrossRef]
56. Olah, G.A. *Friedel-Crafts Chemistry*; Wiley: New York, NY, USA, 1973.
57. Zhang, Y.S.; Hu, L.T.; Zhang, H.; Chen, J.M.; Liu, W.M. Microstructural characterization and crystallization of ZrO_2-Y_2O_3-CuO solid solution powders. *J. Mater. Process. Technol.* **2008**, *198*, 191–194. [CrossRef]